Journal of Marine Research, 69, 57–77, 2011

Secondary instability of salt sheets

by Satoshi Kimura[1,2] and William Smyth[1]

ABSTRACT

In the presence of a vertically varying horizontal current (background shear), the salt-fingering instability is supplanted by the salt-sheet instability. Previous direct numerical simulation (DNS) experiments on salt sheets revealed that flow becomes turbulent via secondary instabilities. We call these instabilities zig-zag and tip modes. Here, we investigate the physics of these modes using linear normal mode stability analysis. As the primary instability (salt-sheet instability) grows, the zig-zag mode emerges, which denotes undulation of growing salt sheets at the center of fingering regions. This mode is shown to be an extension of secondary instability of unsheared two-dimensional salt-fingering. The zig-zag mode is amplifed almost uniformly at all horizontal wavelengths exceeding $O(1\,\mathrm{m})$. This mechanism may, therefore, account for the tilted laminae seen in shadowgraph images of microstructure in salt fingering regions. Subsequently, the tip mode appears at the tips of undulating salt sheets introducing streamwise dependence that leads the flow into turbulent regime.

1. Introduction

Salt-fingering instability can occur when gravitationally stable stratification is maintained by heat, while salt is unstably distributed. Buoyancy anomalies are amplified because the diffusion of heat is more rapid than the diffusion of salt. Where evaporation and surface heating maintain the requisite salinity and temperature gradients (Schmitt, 2003), salt-fingering instability can act to mix heat and salt downward into the ocean interior. Since vertically-sheared, horizontal currents are ubiquitous, it is important that we understand their effects on salt fingering.

Linear theory suggests that salt-fingering can take various planforms, such as sheets, squares, and rectangles (Stern *et al.*, 2001; Schmitt, 1994; Proctor and Holyer, 1986). In the presence of background shear, all planforms with dependence on the streamwise coordinate are damped, so that salt-fingering takes the form of vertical sheets aligned parallel to the flow, the "salt-sheet instability" (Linden, 1974; Smyth and Kimura, 2007). Our focus here is the secondary instabilities that lead salt sheets toward the turbulent state (Kimura and Smyth, 2007).

1. College of Oceanic and Atmospheric Sciences, Oregon State University, Corvallis, Oregon, 97331, U.S.A.
2. Corresponding author. High Cross, Madingley Road, Cambridge CB3 OET, England. ***email: skimura04@gmail.com***

Instabilities of salt sheets are expected to bear some similarity to those of salt fingers, which have been investigated in several previous studies. The secondary instability of salt-fingering was first proposed by Stern as collective instability (Stern, 1969), an oscillatory instability which is an amplification of internal waves on scales much larger than the salt-fingering. Effects of perturbations of all wavelengths were studied in two dimensions by Holyer (1984). Holyer found a small (finger-scale) stationary secondary instability that grows faster than the collective instability. This two-dimensional approximation is of particular relevance here, since the primary salt sheet instability is also two-dimensional. Holyer's calculation treated the vertical velocity induced by salt fingers as a fixed parameter. Stern and Simeonov (2005) assumed instead that the vertical velocity of the finger grows exponentially in time (Stern, 1960, 1975) and found a super exponential mode. Most recently, Traxler *et al.* (2011) utilized the framework of a mean field theory to identify salt-fingering, collective, and layering instabilities.

The secondary stability analyses cited above have not considered the effect of sheared horizontal currents. These studies have also assumed a vertically unbounded fluid domain with uniform stratification. Here, we will employ direct numerical simulations (DNS) and secondary stability analysis to study the transition to turbulence in the presence of vertically varying horizontal current on a localized fingering layer. We will show how Holyer's (1984) mode is altered by the presence of background shear, and also explore the distinct instability that we call tip mode.

Section 2 reviews the DNS model and describes the sequence of secondary instabilities that leads to turbulence in DNS experiments. In Section 3, two distinct instabilities, the zig-zag and tip modes, are identified using linear normal mode stability analysis. Results from secondary stability analysis and DNS are compared in Section 4. In Section 5, instability mechanisms are investigated via the perturbation kinetic energy budget. Conclusions are summarized in Section 6.

2. Direct simulations

The Boussinesq equations are cast in a nonrotating Cartesian coordinate system $\{x, y, z\}$. Buoyancy is assumed to be a linear function of temperature and salinity. The resulting field equations describe the time evolution of the instantaneous velocity field $\vec{u}(x, y, z, t) = \{u, v, w\}$, the thermal component of buoyancy, b_T and the saline components of buoyancy, b_S as

$$\frac{D\vec{u}}{Dt} = -\nabla\pi + b\hat{k} + \nu\nabla^2\vec{u}, \tag{1}$$

$$\nabla \cdot \vec{u} = 0, \tag{2}$$

$$\frac{Db_T}{Dt} = \kappa_T\nabla^2 b_T, \tag{3}$$

$$\frac{Db_S}{Dt} = \kappa_S \nabla^2 b_S, \tag{4}$$

$$b = b_T + b_S. \tag{5}$$

The variable π represents the reduced pressure (pressure scaled by the uniform characteristic density ρ_0). The buoyancy force is parallel to the vertical unit vector, $\hat{k}$. Buoyancy is defined as $b = -g(\rho - \rho_0)/\rho_0$, where g is the acceleration due to gravity in accordance with Boussinesq approximation. The kinematic viscosity of sea water is represented as ν. The variables κ_T and κ_S are the molecular diffusivities of heat and salt, respectively.

The initial profiles of background velocity and stratification represent a stratified double-diffusive shear layer:

$$\frac{u}{\Delta u} = \frac{b_T}{\Delta B_T} = \frac{b_S}{\Delta B_S} = \tanh\left(\frac{z}{h}\right). \tag{6}$$

Here, Δu is the half-change of background velocity across a transition layer of half-depth h. ΔB_T and ΔB_S are the half-changes in thermal and saline buoyancy, respectively. The half-change in total buoyancy is then $\Delta B = \Delta B_T + \Delta B_S$. Boundary conditions are periodic in the horizontal with periodicity intervals L_x and L_y in the streamwise (x) and spanwise (y) directions, respectively. Upper and lower boundaries, located at $z = L_z/2$ and $z = -L_z/2$, are impermeable ($w = 0$) and flux-free ($\partial u/\partial z = \partial v/\partial z = \partial b_T/\partial z = \partial b_S/\partial z = 0$). L_z is the domain height.

Computational resource needs are sensitive to the choice of the diffusivity ratio, $\tau = \kappa_S/\kappa_T$. In the ocean, the molecular diffusion of salt is two orders of magnitude slower than that of heat, i.e., $\tau = 0.01$. Historically, larger values of τ have been used in order to ease resource requirements (e.g. Stern *et al.*, 2001; Gargett *et al.*, 2003; Smyth *et al.*, 2005). Only recently has three-dimensional DNS with $\tau = 0.01$ become possible (Kimura and Smyth, 2007). Secondary stability analysis is even more computationally expensive than DNS.[3] When $\tau = 0.01$, salt sheets develop gradients too sharp to be resolved in secondary stability analysis with the available memory. Accordingly we will choose $\tau = 0.16$ for this experiment.

The numerical code used to solve (1)–(5) is described in Winters *et al.* (2004) with modifications as discussed by Smyth *et al.* (2005) and Kimura and Smyth (2007). Salinity is resolved on a fine grid with spacing equal to one half the spacing used to resolve the other fields. The resulting array dimensions for the fine grid are $(nz, ny, nx) = (768, 20, 576)$.

The density ratio $R_\rho = -\Delta B_T/\Delta B_S$ and bulk (minimum) Richardson number $Ri = \Delta B h/\Delta u^2$ were set to 1.6 and 2.0 respectively. These values were taken from observations of a thermohaline staircase off Barbados (Gregg and Sanford, 1987). The spanwise periodicity interval L_y was chosen so as to accommodate one wavelength of the fastest-growing

3. While the memory requirement for DNS scales as N^3, where N is a typical array dimension, the matrix whose eigenvalues and eigenvectors describe secondary instabilities has size $N^2 \times N^2 = N^4$. Processing time for DNS scales as N^4 (accounting for the Courant-Friedrichs-Leowy timestep limitation), whereas the time needed for the eigenvalue analysis is $\sim (N^2)^3 = N^6$.

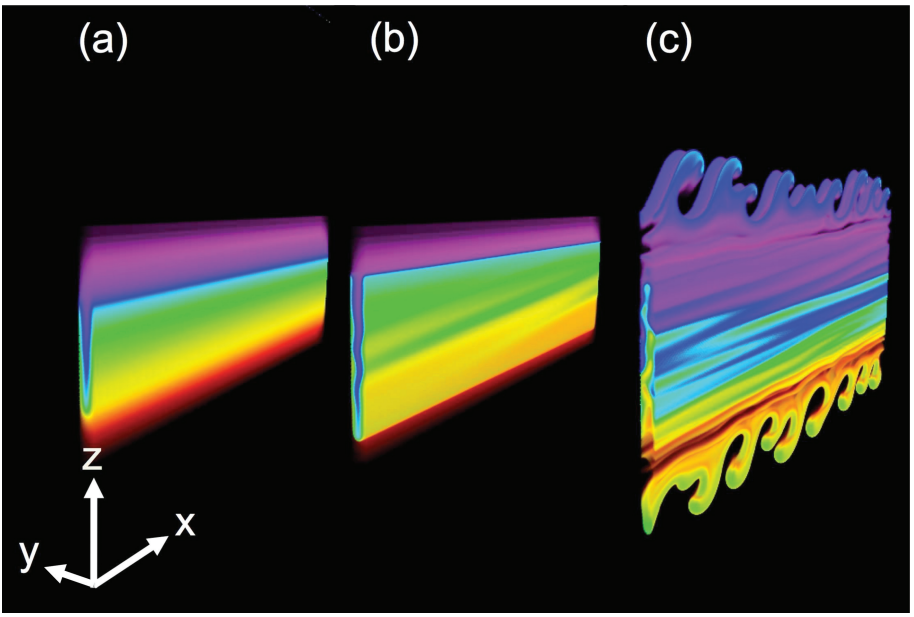

Figure 1. The saline buoyancy is color coded. Values range from $-0.21\Delta B_S$(blue) to $+0.21\Delta B_S$(red), with values outside that range rendered transparent. (a): Snapshot at 3030 s shows the primary instability at finite amplitude. (b): Snapshot at 4132 s shows the zig-zag mode (buckling of the salt sheets). (c): Snapshot at 5923 s shows the tip mode (ripples with short wavelength at the top and bottom of the salt sheets).

primary instability (e.g. Stern, 1960, 1975; Smyth and Kimura, 2007). The possibility of subharmonic secondary instabilities spanning two or more salt sheets can be included via Floquet analysis. The appropriate value for L_x is not well known *a priori*. Sensitivity tests showed no significant dependence of secondary instability characteristics on L_x. We used $L_x = 1.5\,\mathrm{m}$, $L_y = 0.04\,\mathrm{m}$ and $L_z = 1.9\,\mathrm{m}$. L_z is larger than the layer half-thickness, $h = 0.31\,\mathrm{m}$, by a factor of 6, so upper and lower boundaries are expected to have little influence on the flow evolution.

Figure 1 shows three snapshots of the evolving saline buoyancy field. In Figure 1a, planar regions of rising and sinking motions generate spanwise gradients in salinity; this is the primary instability, salt-sheet instability. As the primary instability grows, salt sheets start to undulate at mid-depth in the y direction. This motion appears to be related to the secondary instability found in unsheared, unbounded, salt fingers (Holyer, 1984; Stern and Simeonov, 2005). [Both Holyer (1984) and Stern and Simeonov (2005) considered two-dimensional salt fingers, and their x and z coordinates correspond to our y and z coordinates.] We call this secondary instability the zig-zag mode (Fig. 1b). At this stage, the x dependence is relatively weaker than the dependence on y and z, and the basic background states can be

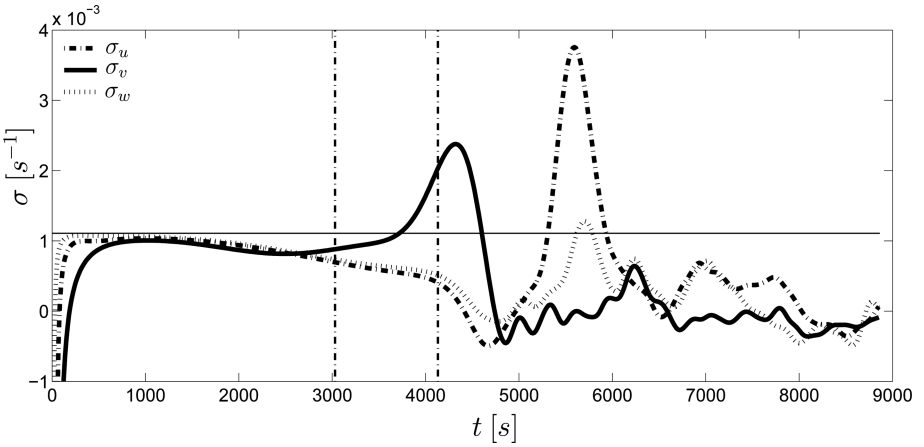

Figure 2. Evolution of growth rates as defined in Eq. (8) from DNS. The horizontal line indicates the primary growth rate σ_{LS} calculated from primary stability analysis described by Smyth and Kimura (2007). Vertical dashed lines indicate $t = 3030$ s and $t = 4132$ s, the times chosen as base states for the stability analyses to be discussed in Section 3.

well described as a function of y and z (Figs. 1a and 1b). Finally, secondary instability introduces quasiperiodic dependence on x (Fig. 1c). The x-dependence has the strongest signals at the top and bottom tips of the salt sheets; therefore, we identify this motion as the tip mode. The x-dependence resembles the shear-tilted salt fingers observed by Kunze *et al.* (1987), using optical microstructure from a free-fall shadowgraph profiler in the water column east of Barbados. This secondary circulation leads the flow into the turbulent regime.

Secondary instability growth is now analyzed using an instantaneous exponential growth rate for the velocity fluctuations. The velocity fluctuations are defined as

$$\vec{u}'(x, y, z, t) = \vec{u}(x, y, z, t) - < \vec{u}(x, y, z, t) >_{xy} \tag{7}$$

where the subscripted angle bracket indicates the average over horizontal directions. Exponential growth rates for the velocity perturbation components are defined as

$$\sigma_u = \frac{1}{2}\frac{d}{dt} \ln < u'^2 >_{xyz}; \quad \sigma_v = \frac{1}{2}\frac{d}{dt} \ln < v'^2 >_{xyz}; \quad \sigma_w = \frac{1}{2}\frac{d}{dt} \ln < w'^2 >_{xyz} . \tag{8}$$

Angle brackets and subscript denote an average over all three directions.

Evolution of the growth rates is shown in Figure 2. As expected, the initial perturbations quickly adjust to a state in which all three growth rates approach σ_{LS} (horizontal line), the growth rate of the primary salt sheet instability. After a period of slow decrease, we observe a peak of the spanwise velocity growth (solid curve in Figure 2, at $t \approx 4400$ s), followed by a peak in the streamwise growth rate (dashed curve in Figure 2, at $t \approx 5600$ s). The same sequence of the events has been reported for the more realistic case, $\tau = 0.01$ (Kimura and Smyth, 2007). These two distinct peaks indicate the presence of secondary instabilities.

Secondary stability analysis of salt-fingering by Stern and Simeonov (2005) considered the effect of the evolving mean flow and found superexponential growth. In our study, the presence of the mean streamwise velocity makes it difficult to account for the time evolution of the mean flow in the stability analysis. Instead, for the purpose of the secondary stability analysis, we assume that the background flow does not change with respect to time, i.e. we make the frozen flow approximation. Change in the mean flow over time will eventually affect the evolution of the perturbation but, if that change is sufficiently slow, the approximation is valid.

The time scales for mean flow evolution and perturbation growth are now compared to justify the use of the frozen flow approximation. The time scale for mean flow evolution is defined, somewhat arbitrarily, as the interval over which the largest growth rate is larger than σ_{LS} (Fig. 2). The e-folding time for the perturbation is the reciprocal of the growth rate. The time scales for the mean flow during the two intervals of secondary instability growth are 1010 s and 625 s. The e-folding times for the same two intervals are 533 s and 297 s, respectively. In both instabilities, the perturbation growth rate is of the same order of magnitude as the rate of mean flow evolution. Therefore the frozen flow approximation is marginally valid, and a practical first step toward a more thorough analysis.

3. Secondary stability analysis

We hypothesize that the growth of the salt sheets to finite amplitude drives the secondary instability. We therefore define a background flow that includes the salt sheets by applying an average over streamwise (x) direction to the DNS fields. The velocity, buoyancy and pressure terms are then separated into two parts, the background state (upper case) and a perturbation (lower case with primes),

$$\vec{u} = U(y,z)\hat{i} + V(y,z)\hat{j} + W(y,z)\hat{k} + \epsilon\vec{u'}(x,y,z,t); \tag{9}$$

$$b_T = B_T(y,z) + \epsilon b'_T(x,y,z,t); \tag{10}$$

$$b_S = B_S(y,z) + \epsilon b'_S(x,y,z,t); \tag{11}$$

$$\pi = \Pi(y,z) + \epsilon\pi'(x,y,z,t). \tag{12}$$

Our objective is to investigate the growth of the perturbations. The mean buoyancy, $B(y,z)$ is defined as $B(y,z) = B_T(y,z) + B_S(y,z)$. We substitute (9)–(12) into (1)–(5) and collect the $O(\epsilon)$ terms:

$$\frac{\partial u'}{\partial t} + \left[U\frac{\partial}{\partial x} + V\frac{\partial}{\partial y} + W\frac{\partial}{\partial z}\right]u' + \left[v'\frac{\partial}{\partial y} + w'\frac{\partial}{\partial z}\right]U = -\frac{\partial \pi'}{\partial x} + \nu\nabla^2 u', \tag{13}$$

$$\frac{\partial v'}{\partial t} + \left[U\frac{\partial}{\partial x} + V\frac{\partial}{\partial y} + W\frac{\partial}{\partial z}\right]v' + \left[v'\frac{\partial}{\partial y} + w'\frac{\partial}{\partial z}\right]V = -\frac{\partial \pi'}{\partial y} + \nu\nabla^2 v', \tag{14}$$

$$\frac{\partial w'}{\partial t} + \left[U\frac{\partial}{\partial x} + V\frac{\partial}{\partial y} + W\frac{\partial}{\partial z}\right]w' + \left[v'\frac{\partial}{\partial y} + w'\frac{\partial}{\partial z}\right]W = -\frac{\partial \pi'}{\partial z} + b_T' + b_S' + \nu\nabla^2 w', \tag{15}$$

$$\frac{\partial u'}{\partial x} + \frac{\partial v'}{\partial y} + \frac{\partial w'}{\partial z} = 0, \tag{16}$$

$$\frac{\partial b_T'}{\partial t} + \left[U\frac{\partial}{\partial x} + V\frac{\partial}{\partial y} + W\frac{\partial}{\partial z}\right]b_T' + \left[v'\frac{\partial}{\partial y} + w'\frac{\partial}{\partial z}\right]B_T = \kappa_T\nabla^2 b_T', \tag{17}$$

$$\frac{\partial b_S'}{\partial t} + \left[U\frac{\partial}{\partial x} + V\frac{\partial}{\partial y} + W\frac{\partial}{\partial z}\right]b_S' + \left[v'\frac{\partial}{\partial y} + w'\frac{\partial}{\partial z}\right]B_S = \kappa_S\nabla^2 b_S'. \tag{18}$$

A diagnostic equation for the pressure,

$$\nabla^2\pi' = -2\frac{\partial v'}{\partial x}\frac{\partial U}{\partial y} - 2\frac{\partial w'}{\partial x}\frac{\partial U}{\partial z} - 2\frac{\partial v'}{\partial y}\frac{\partial V}{\partial y} - 2\frac{\partial v'}{\partial z}\frac{\partial W}{\partial y} - 2\frac{\partial w'}{\partial y}\frac{\partial V}{\partial z} - 2\frac{\partial w'}{\partial z}\frac{\partial W}{\partial z} + \frac{\partial b_T'}{\partial z} + \frac{\partial b_S'}{\partial z}, \tag{19}$$

is obtained by applying $\nabla\cdot$ to (13)–(15) and using (16). Note that (13) decouples from the other equations, so that the sytem to be solved is (14), (15), (17), (18) and (19).

The perturbations are assumed to have the same spanwise periodicity as the salt sheets, and take the normal mode form:

$$\phi(x, y, z, t) = e^{\sigma t + ikx}\sum_{n=-(N-1)/2}^{(N-1)/2}\sum_{m=0}^{M}\hat{\phi}_{n,m}F_m(z)e^{i\left(\frac{2n\pi}{L_y} + \mu\frac{2\pi}{L_y}\right)y}; \tag{20}$$

The variable ϕ stands for any of the perturbations, u', v', w', b_T', b_S', and π', where k is the real streamwise wavenumber and $\sigma = \sigma_r + i\sigma_i$ is the complex exponential growth rate of the perturbation. The vertical structure functions are given by

$$F_m(z) = \cos\left(\frac{m\pi}{L_z}\left(z - \frac{L_z}{2}\right)\right) \text{ for } u', v', \text{ and } \pi'; \tag{21}$$

$$F_m(z) = \sin\left(\frac{m\pi}{L_z}\left(z - \frac{L_z}{2}\right)\right) \text{ for } w', b_T', \text{ and } b_S'. \tag{22}$$

Boundary conditions for the vertical structure functions are flux-free ($u_z' = v_z' = \pi_z' = 0$) and impermeable ($w' = b_T' = b_S' = 0$) at the upper and lower boundaries.

The Floquet parameter μ is used to account for subharmonic modes. A matrix eigenvalue problem is obtained by combining the equations (14), (15), (17), (18) and (19) with (20):

$$\sigma\hat{x} = A\hat{x}, \tag{23}$$

where σ is the eigenvalue, A is the stability matrix and $\hat{x}$ is the concatenation of the disturbances, $\hat{v}_{n,m}$, $\hat{w}_{n,m}$, $\hat{b_T}_{n,m}$ and $\hat{b_S}_{n,m}$. The parameters M and N determine vertical and

spanwise resolution levels, respectively. The eigenvalue problem in (23) is solved using the LAPACK subroutines (Anderson *et al.*, 1999), as provided in the MATLAB software package.

The background flow, U, V, W, B_T and B_S was defined from spanpshots of the DNS results. To account for the evolution of the background flow (which is assumed to be slow compared with instability growth), we perform the stability analysis at two separate times: $t = 3030$ s and $t = 4132$ s (see Fig. 2). The primary salt-sheet instability has reached the finite amplitude at $t = 3030$ s. The subsequent undulation of the salt sheet is relatively uniform in streamwise direction until $t = 4132$ s (Figs. 1b and 2).

An accurate representation of the mean flow is $(M, N) = (384, 11)$, matching the coarse grid resolution of the DNS; however, calculation of multiple growing modes at this resolution is impractical. Instead, the calculation of multiple modes was done with $(M, N) = (192, 11)$. The maximum relative error between the high and low resolution was 7%. For the subharmonic modes, we have varied $\mu = 0, \frac{1}{2}, \frac{1}{3}$, and $\frac{1}{4}$.

We found two distinct modes corresponding to the zig-zag and tip modes identified in Section 2. When the stability analysis is performed at $t = 3030$ s, the fastest-growing mode (FGM) is the zig-zag mode. The zig-zag mode is nonoscillatory ($\sigma_i = 0$) and has maximum growth rate when $k = 0$ and $\mu = 0$. The real part of the growth rate diminishes very little between $k = 0$ and $k = 2\pi/L_x$ (Figs. 3a and 3b). This range includes the gravest mode of our DNS domain, and we are therefore not surprised to find x-dependence with that wavelength in the DNS expression of the zig-zag mode (Fig. 1b). The amplification of the zig-zag mode at all horizontal wavelengths exceeding $O(1\,\mathrm{m})$ (Fig. 3a) may account for the tilted laminae seen in shadowgraph images of microstructure in salt-fingering regions described in Kunze *et al.* (1987).

When the flow field from DNS at 4132 s was used as a background flow, growth rates peak at $k = 52\,\mathrm{m}^{-1}$ for both cases $\mu = 0$ and $\mu = 1/2$ (Fig. 4a). Both modes are strongly oscillatory, with $\sigma_i = 39 \times 10^{-3}\,\mathrm{s}^{-1}$, an order of magnitude larger than σ_r. The phase speed of these modes is, $-\sigma_i/k = -7.5 \times 10^{-4}\,\mathrm{m\,s}^{-1}$. This is between zero and $-\frac{\Delta u}{2}$, indicating a critical level in the lower half of the shear layer. Not shown here is the complex conjugate mode, which has equal growth rate, and opposite phase velocity, relative to the mode shown and is focused in the upper half of the layer.

At $k = 52\,\mathrm{m}^{-1}$, FGM of $\mu = 0$ has a slightly larger growth rate than that of $\mu = 1/2$ (see Fig. 4a); the relative difference between these two growth rates is 4%. Because the maximum relative error caused by this resolution is 7%, FGM of $\mu = 0$ and $\mu = 1/2$ are indistinguishable in our secondary stability analysis. We next compare the spatial structures of the eigenmodes with perturbations seen in the DNS.

4. Comparison with DNS

We next compare the spatial structures of the eigenmodes with perturbations seen in the DNS. Results from secondary stability analysis suggest that the zig-zag mode emerges

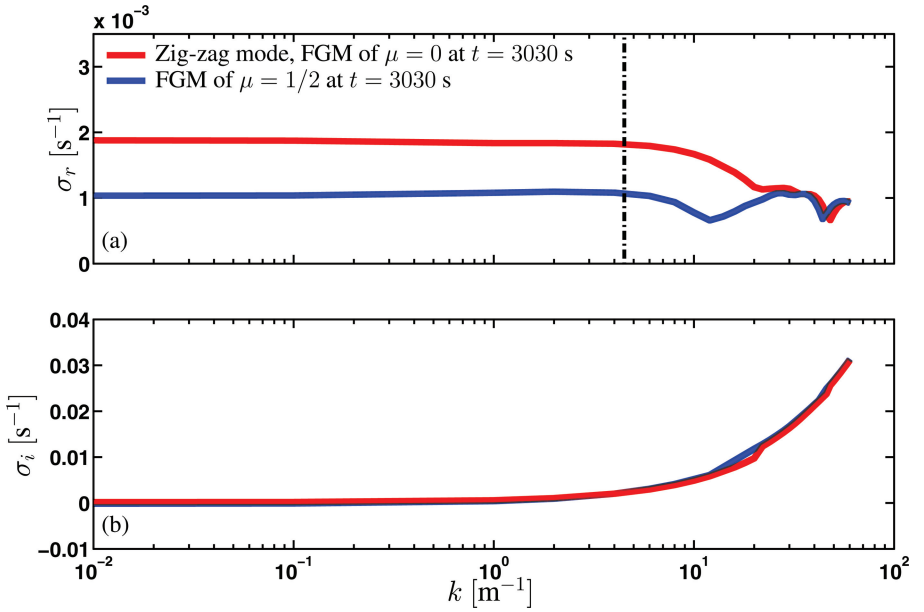

Figure 3. Real parts of growth rates (a) and imaginary part of growth rates (b) versus streamwise wavenumber for the zig-zag and subharmonic modes. When the background flow from DNS at $t = 3030$ s is used, the fastest growing mode (FGM) is the zig-zag mode. The vertical dashed line on (a) indicates $2\pi/L_x$, the gravest horizontal mode for the DNS.

before the tip mode (Figs. 3 and 4). Accordingly, the zig-zag mode and tip modes are compared with DNS data at 4132 s and 5923 s.

We compared the spanwise perturbation velocity from DNS at 4132 s with the secondary stability analysis result at $k = 0$. Both Figures 5a and 5b show a stack of left and right going layers that cause the buckling of the salt sheets. The vertical dependence (both wavelength and envelope) is similar in the stability analysis and the DNS, but the vertical wavelength of the normal mode instability is variable and is generally larger than that seen in the DNS. This is likely an artifact of the frozen flow approximation made in the stability analysis.

The spanwise wavelength of ripples at the top edges of salt sheets corresponds to twice the wavelength of single salt sheet (Fig. 6). This suggest that FGM of $\mu = 1/2$ will dominate over $\mu = 0$. Streamwise dependence introduced by the tip mode is verified by the DNS data at the times of peak streamwise and vertical growth seen in Figure 2: 5923 s. The secondary stability analysis shows maximum growth rate at $k = 52\,\mathrm{m}^{-1}$, so the predicted wavelength is $2\pi/k = 0.1$ m. This wavelength corresponds with the ripples at the top and bottom of the salt sheets at 5923 s to within a few tens of percent (see Fig. 7). The eigenfunction (not shown, though see Figures 10a and 10b in the following section) has energy concentrated near the tips of the salt sheets, as expected.

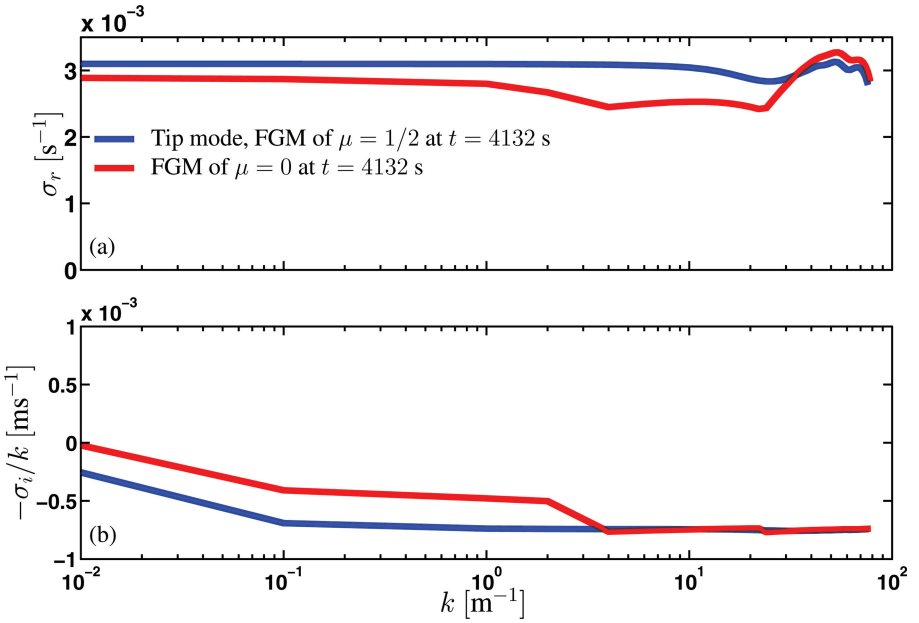

Figure 4. Real parts of growth rates (a) and phase speed (b) versus streamwise wavenumber for the tip and FGM of $\mu = 0$. The background flow from DNS at $t = 4132$ s is used.

We conclude that the spatial structures of the modes at $k = 0$ and $k = 52\,\mathrm{m}^{-1}$ correspond well with the zig-zag and tip modes seen in the DNS, given the limitations of spatial resolution and the frozen flow approximation.

5. Mechanisms of secondary instability

As an initial hypothesis, one might imagine that both zig-zag and tip modes are a combination of shear and buoyancy driven instabilities. The primary salt-sheet instability is the alternation of rising and sinking motions that varies in the y direction (see Fig. 1a). This geometry suggests that the undulation of salt sheets is due to a shear instability driven by the y-dependence of the background vertical velocity. This supposition has underlain attempts to parameterize fluxes due to salt fingers (e.g. Kunze, 2003). In addition, faster diffusion of heat relative to salt creates regions of gravitationally unstable fluid at the extremities of the salt sheets, suggesting convective instability, while lateral buoyancy gradients between salt sheets may support sloping convection.

A shear instability driven by $\partial W/\partial y$ may be described approximately by a solution of Rayleigh's equation with a sinusoidal profile of background velocity $W = W_0 \sin(k_y y)$. A numerical solution for this case (Hazel, 1972) yields a fastest-growing mode with wavenumber equal to $k_y/1.8$. In other words, the z-wavelength of the shear instability is predicted

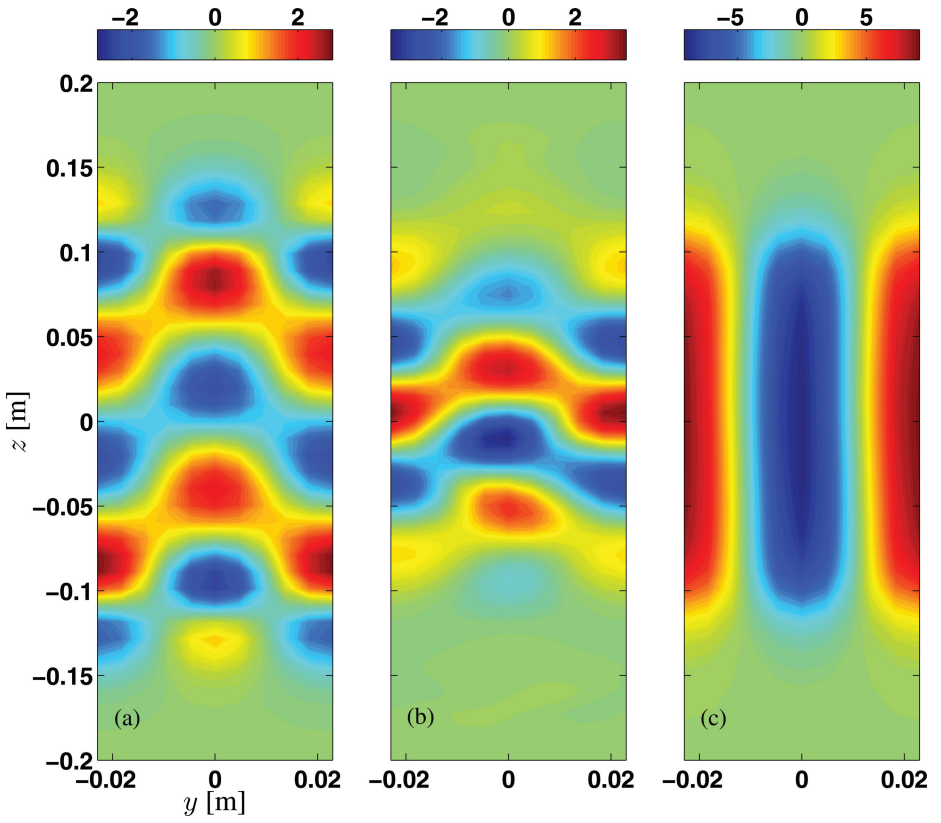

Figure 5. (a) $Re[v'(y, z)]$ from the secondary stability analysis. (b) $v'(y, z, x = 0)$ from DNS 4132 s (c) Mean $W \times 10^5$ at DNS 3030 s.

to exceed the y-wavelength of the salt sheets by a factor 1.8. In the related case of two-dimensional unsheared salt fingers, the secondary instability has wavelength in the z direction $1.7 - 1.8$ times of the original wavelength of salt fingers over a wide range of parameter values (Stern and Simeonov, 2005). This correspondence with Hazel (1972) is consistent with the possibility that the undulation of salt fingers is driven by the periodic shear of the vertical motions of salt fingers. The picture is complicated, however, by the effect of viscosity. The Reynolds number computed on the scales of the salt sheet is $O(1)$, small enough to quench shear instability. An alternative possibility to be investigated below is sloping convection driven by the lateral buoyancy gradients between adjacent salt sheets.

The tips of the salt sheets are regions of vertical convergence, and thus exhibit sharp gradients of both horizontal velocity and buoyancy. This localized shear layer can be susceptible to Kelvin-Helmholtz instability, which creates quasi-periodic dependence on x. Alternatively, faster diffusion of heat relative to salt creates regions of gravitationally unstable fluid

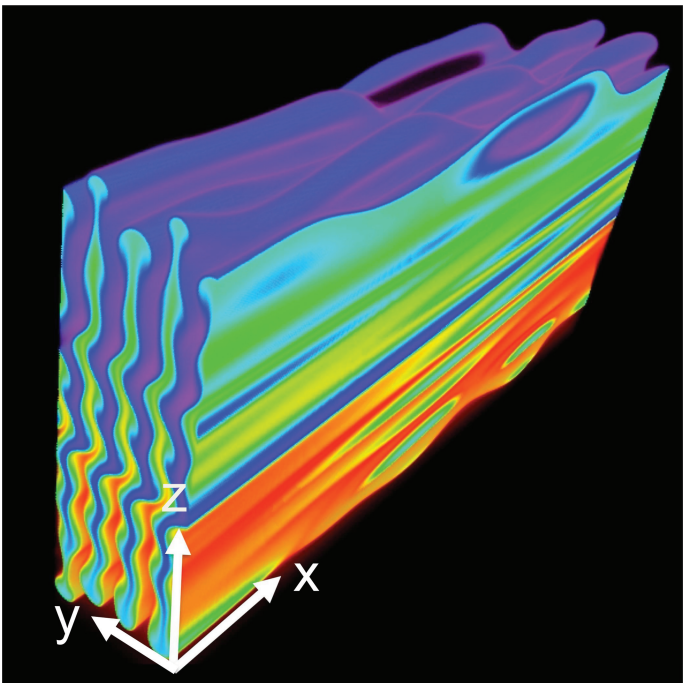

Figure 6. A snapshot of saline buoyancy field from DNS initialized with four salt sheets at $t = 5923$ s. Values range from $-0.21\Delta B_S$(blue) to $+0.21\Delta B_S$(red), with values outside that range rendered transparent. The growth of salt sheets at the top edges are not uniform in y. Instead, every other salt sheets has the same height, i.e, the growth of salt sheets create the spanwise disturbance that is doubled the wavelength of single salt sheet.

at the extremities of the salt sheets. The resulting convective cells could pinch the fluid at the tips, creating blobs of unstable fluid, which is seen in DNS of unsheared salt fingers (Shen, 1995).

In an attempt to quantify the relative importance of buoyancy and shear forcing, we analyzed the sources of perturbation kinetic energy, defined as

$$K_e(y, z, t) = \frac{1}{2} < \vec{u'} \cdot \vec{u'} >_x . \tag{24}$$

The time rate of change in perturbation kinetic energy is obtained by taking the scalar product of $\vec{u'}$ with the momentum equations (13)–(15). The resulting equation is

$$\frac{\partial K_e}{\partial t} + \nabla \cdot F = Sh + B + \epsilon_d, \tag{25}$$

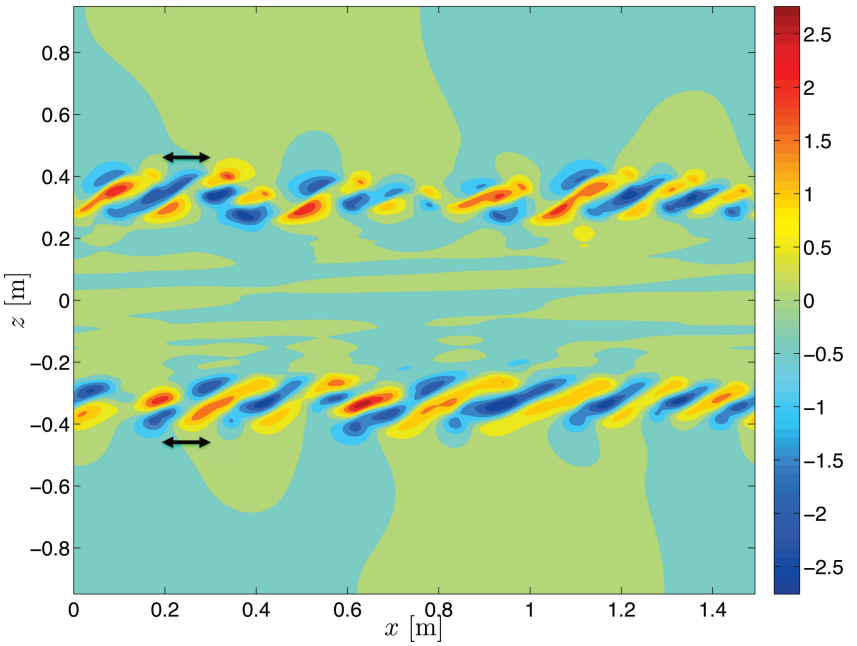

Figure 7. Streamwise velocity perturbation, $u'(x, y = 0, z, t = 5923\,s) \times 10^4$, in color from DNS. Arrows at the tip and bottom indicate the wavelength, 0.1 m, predicted for the tip mode.

where

$$Sh = -\left\langle u'v'\frac{\partial U}{\partial y}\right\rangle_x - \left\langle u'w'\frac{\partial U}{\partial z}\right\rangle_x - \left\langle v'v'\frac{\partial V}{\partial y}\right\rangle_x - \left\langle v'w'\frac{\partial V}{\partial z}\right\rangle_x - \left\langle w'v'\frac{\partial W}{\partial y}\right\rangle_x - \left\langle w'w'\frac{\partial W}{\partial z}\right\rangle_x ; \tag{26}$$

$$B = \left\langle w'b'_T\right\rangle_x + \left\langle w'b'_S\right\rangle_x ; \tag{27}$$

$$\epsilon_d = -2\nu < e_{i,j}e_{i,j} >_x ; \quad e_{ij} = \frac{1}{2}\left(\frac{\partial u'_i}{\partial x_j} + \frac{\partial u'_j}{\partial x_i}\right). \tag{28}$$

The expressions Sh, B and ϵ_d represent the shear production, buoyancy production and dissipation respectively. The second term on the left-hand side of (25) is the divergence of a sum of advective, pressure-driven and viscous fluxes. We will not consider this term since it vanishes when the spatial average is taken.

The evolution of perturbation kinetic energy budget over time is analyzed using an instantaneous exponential growth rate for the velocity fluctuations:

$$\sigma_{Total} = \frac{1}{2 < K_e >_{yz}} \frac{d < K_e >_{yz}}{dt}. \tag{29}$$

The relative importance of the physical processes described by the individual terms on the right-hand side of (25) is quantified using partial growth rates of the form

$$\sigma_S = \frac{< Sh >_{yz}}{2 < K_e >_{yz}} \tag{30}$$

and similarly for the buoyancy, σ_B and the dissipation, σ_d. The K_e budget can then be written as

$$\sigma_{Total} = \sigma_S + \sigma_B + \sigma_d. \tag{31}$$

Because σ_d is negative definite, the perturbation kinetic energy can only be supplied by the shear and buoyancy production terms.

Individual terms of σ_S and σ_B can be written as

$$\sigma_S = \sigma_{uv} + \sigma_{uw} + \sigma_{vv} + \sigma_{vw} + \sigma_{wv} + \sigma_{ww}, \tag{32}$$

$$\sigma_B = \sigma_{wt} + \sigma_{ws}. \tag{33}$$

These individual terms take the form of (30), where the numerator is replaced by the individual shear and buoyancy production terms described in (26) and (27).

a. Shear production mechanisms

Since we considered the background velocity of U, V, and W with y and z dependence, there are six shear production terms described in (32). We will identify the dominant component of the shear production term for the zig-zag and tip modes.

In the case of the zig-zag mode, the largest contribution to the shear production is made by σ_{wv} (Fig. 8a). This is consistent with the hypothesis that the zig-zag mode is amplified by the spanwise variation of the mean vertical velocity, as described at the beginning of this section. The second-largest term, σ_{uw}, describes the growth of streamwise velocity fluctuations as the mean flow $U(y, z)$ is advected by the zig-zag mode. These two dominant shear production terms have quasiperiodic form within the interior of the salt sheets (Fig. 9).

In the tip mode, conversion from the mean to perturbation kinetic energy is dominated by σ_{ww} and σ_{uw} (Fig. 8b). The largest term σ_{ww} suggests that the straining of the perturbation vertical velocity by the vertical convergence $\partial W/\partial z < 0$ near the extremities of the salt

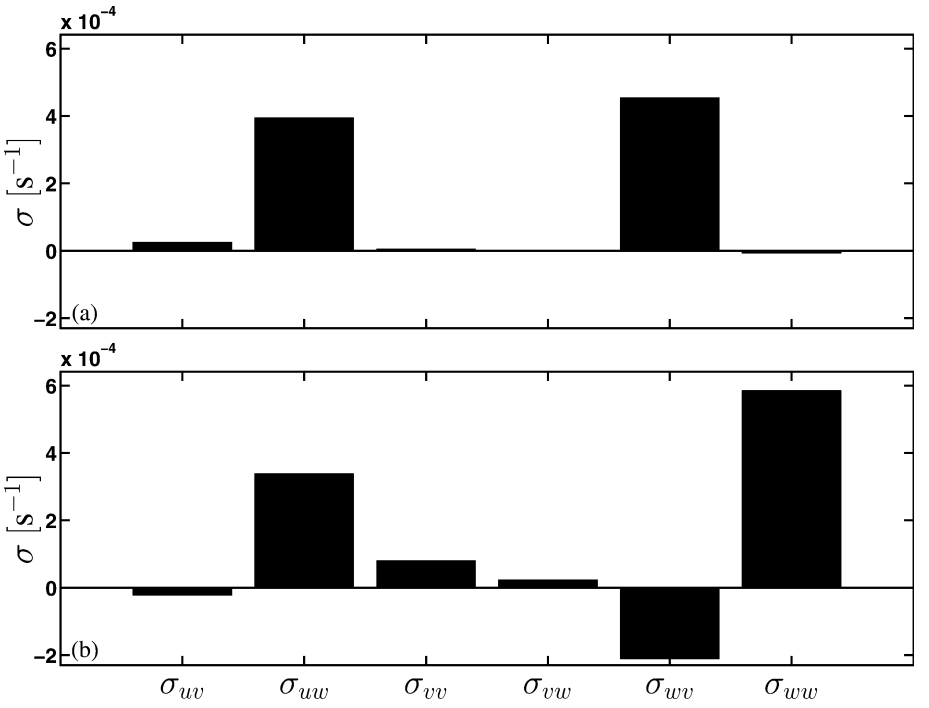

Figure 8. Partial growth rates of individual shear production terms for the zig-zag mode (a) and tip mode (b).

sheets generates perturbation kinetic energy. In contrast, straining does not play a significant role in the zig-zag mode. The second largest term, σ_{uw} is the interaction between Reynolds stress, $< u'w' >_x$ and the ambient shear $\partial U/\partial z$. The two dominant shear production terms have signals concentrated at the bottom edge of the growing salt sheets (Figs. 10a and 10b). The conjugate mode (not shown here) has signals concentrated at the top edge. None of the dominant shear production terms in the tip mode has a signal in the interior of the salt sheets.

b. Buoyancy production mechanisms

An alternative mechanism for instability growth is convection as quantified by the buoyancy production term $\sigma_B = \sigma_{wt} + \sigma_{ws}$. The mean buoyancy is unstably distributed at the tips of salt sheets (Fig. 11a). The zig-zag mode is focused in the regions of strong lateral density gradients where sloping convection is possible (Fig. 11b). The tip mode has the strongest buoyancy production in the regions of strong vertical density gradients (Fig. 11c).

In both cases, the net growth rate σ_T represents a small imbalance between amplification by shear and buoyancy and dissipation by viscosity (Fig. 12). In each case, buoyancy

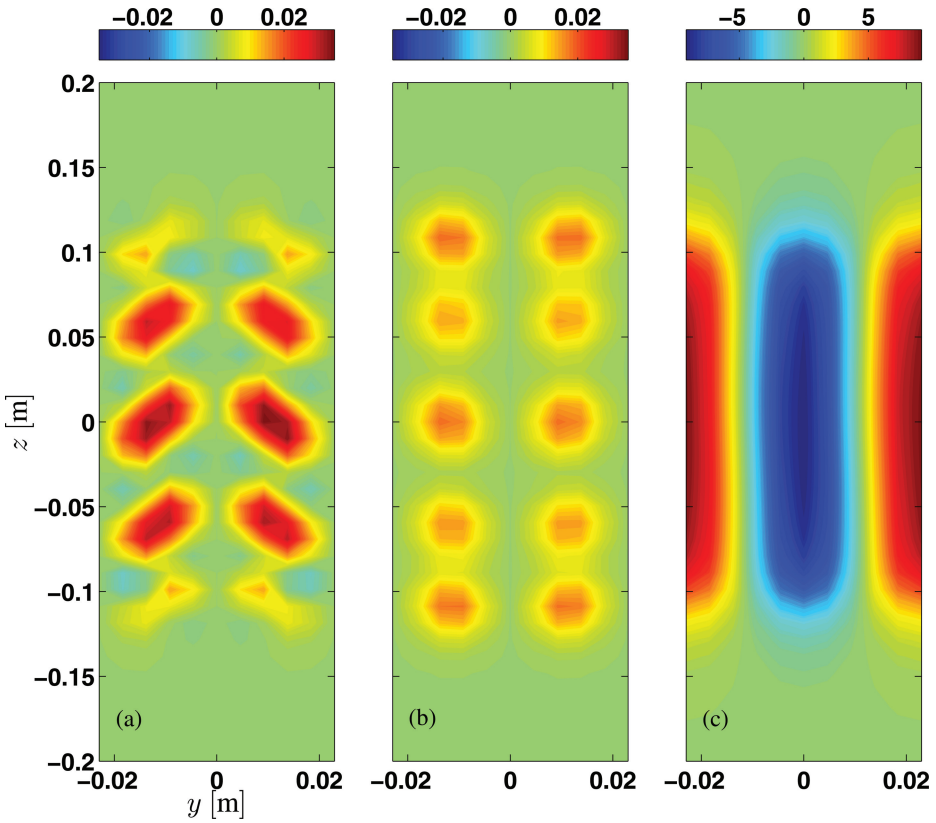

Figure 9. (a) $\left\langle -w'v'\frac{\partial W}{\partial z}\right\rangle_x$ zig-zag mode. (b) $\left\langle -u'w'\frac{\partial U}{\partial z}\right\rangle_x$ zig-zag mode (c) Mean $W \times 10^5$ at DNS 3030 s.

production is an order of magnitude stronger than the shear production. The thermal buoyancy production for the zig-zag and tip modes is negative $\sigma_{wt} = -0.014\,\mathrm{s}^{-1}$ and $\sigma_{wt} = -0.013\,\mathrm{s}^{-1}$, while the saline buoyancy production is positive $\sigma_{ws} = 0.025\,\mathrm{s}^{-1}$ and $\sigma_{ws} = 0.021\,\mathrm{s}^{-1}$. Thus, the buoyancy production represents the release of gravitational potential energy stored in the saline buoyancy.

This is a noteworthy result, especially for the zig-zag mode, whose wavelength corresponds so well with that of shear instability. One must suspect that the dominance of buoyancy production is in some sense an artifact of the assumptions that underlie our normal mode stability analyses, i.e. that small-amplitude perturbations grow on a frozen background flow. To check this, we compute the analogous production terms in the DNS output, where the assumptions of linear normal mode theory are not made. The partial growth rates due to shear and buoyancy production for DNS are calculated using (32) and (33), as for the eigenmodes. Figure 13 shows that the buoyancy production dominates over

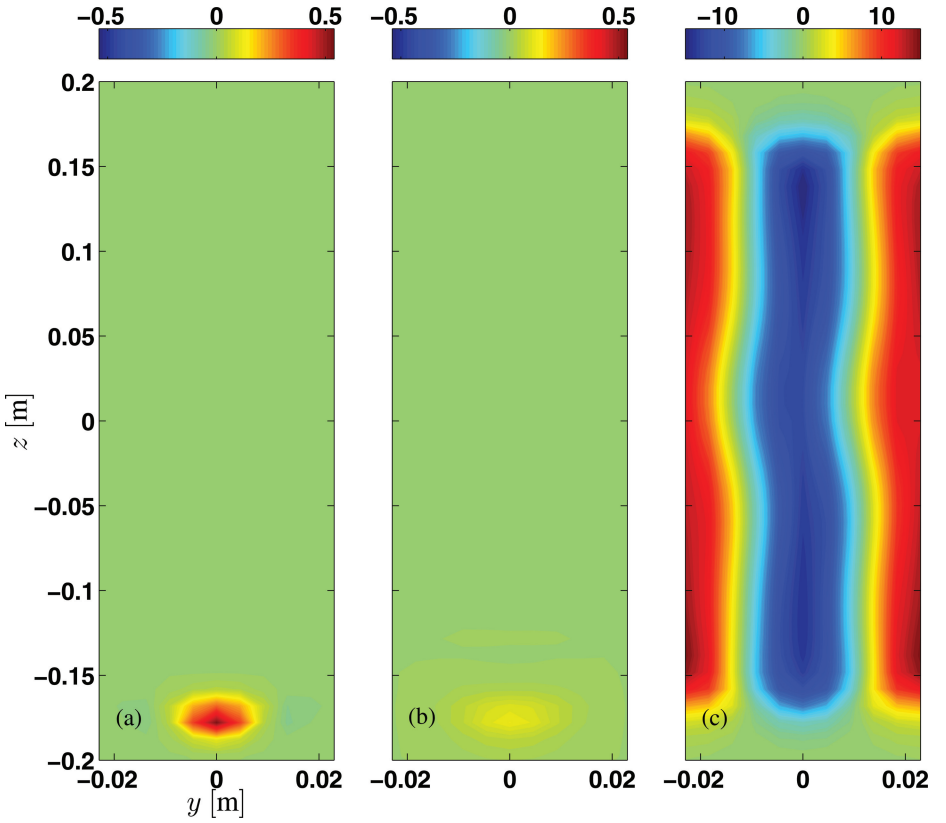

Figure 10. (a) $\left\langle -w'w'\frac{\partial W}{\partial z}\right\rangle_x$ tip mode. (b) $\left\langle -u'w'\frac{\partial U}{\partial z}\right\rangle_x$ tip mode. (c) Mean $W \times 10^5$ at DNS 4132 s.

the shear productions after $t = 3030$ s. We conclude that the dominance of the buoyancy production is not an artifact of either linearization or the frozen flow approximation.

6. Conclusions

DNS of salt sheets revealed the secondary instabilities, which we call the zig-zag and tip mode. We examined the zig-zag and tip mode via linear normal mode secondary stability analysis. We have also discussed mechanisms of these modes as quantified by the perturbation kinetic energy budget. While our simulation and stability analysis are intended to shed light on secondary instabilities of oceanic salt sheets, the following caveats should be noted: the ratio of molecular diffusivity of salt to heat is larger than the ocean; the half-layer thickness is at least smaller than observed thickness; the equation of state is linear; the background flow is assumed to be constant in time for our linear normal mode stability analysis, the frozen flow approximation.

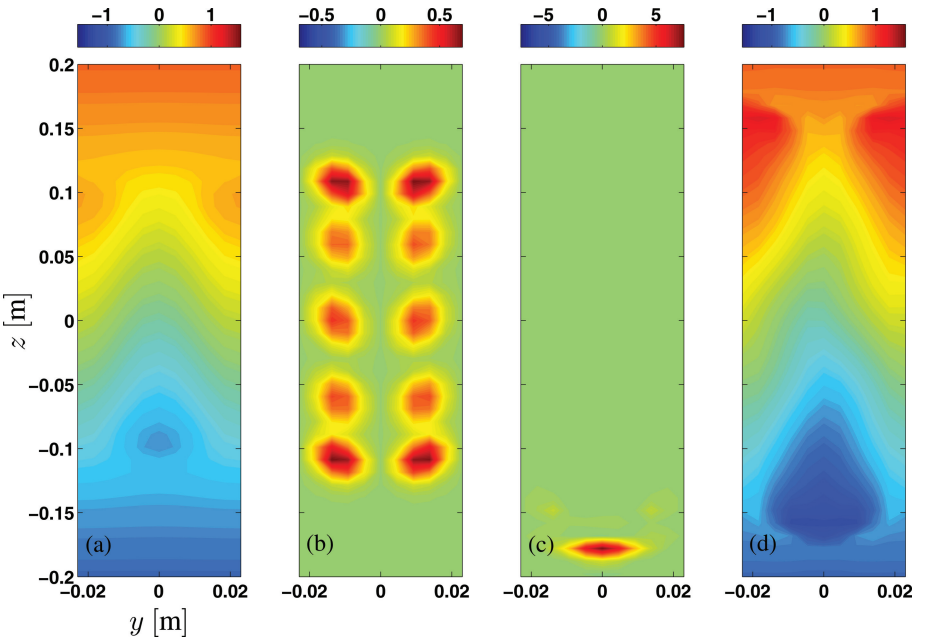

Figure 11. (a) Mean $B \times 10^5$ at DNS 3030 s. Red indicates the positive buoyancy and blue is for the negative buoyancy. (b) $< w'b' >_x$ zig-zag mode. (c) $< w'b' >_x$ tip mode. (d) Mean $B \times 10^5$ at DNS 4132 s.

Our main findings are as follows:

- The zig-zag mode is a three-dimensional analogue of the stationary secondary instability found in two-dimensional analysis of salt fingers (e.g. Holyer, 1984, 1985; Veronis, 1987; Stern and Simeonov, 2005). Although the zig-zag mode grows fastest at $k = 0$, it has nearly equal growth rate from $k = 0$ to $k = 10\,\mathrm{m}^{-1}$ (Fig. 3), suggesting amplification over all horizontal scales exceeding ~1 m. We suggest that this accounts for the tilted laminae seen in the shadowgraph images of Kunze (1987).
- The largest contributions to the perturbation kinetic energy of the zig-zag mode are made by $< w'b' >_x$ and $\left\langle -w'v' \frac{\partial W}{\partial y} \right\rangle_x$. The buoyancy production $< w'b' >_x$ coincides with strong lateral density gradients, suggesting sloping convection.
- The tip mode is an oscillatory instability with dependence on the streamwise direction. The largest contributions to the perturbation kinetic energy of the tip mode were made by $< w'b' >_x$ and $\left\langle -w'w' \frac{\partial W}{\partial z} \right\rangle_x$. Both the shear and buoyancy production are concentrated at the tips of growing salt sheets where the vertical buoyancy gradient is unstable. This mode may represent the three-dimensional analogue of the pinch-off process described by Shen (1995).
- For both zig-zag and tip modes, perturbation energy growth is driven mainly by the buoyancy production. Dominance of buoyancy forcing has been confirmed in the DNS

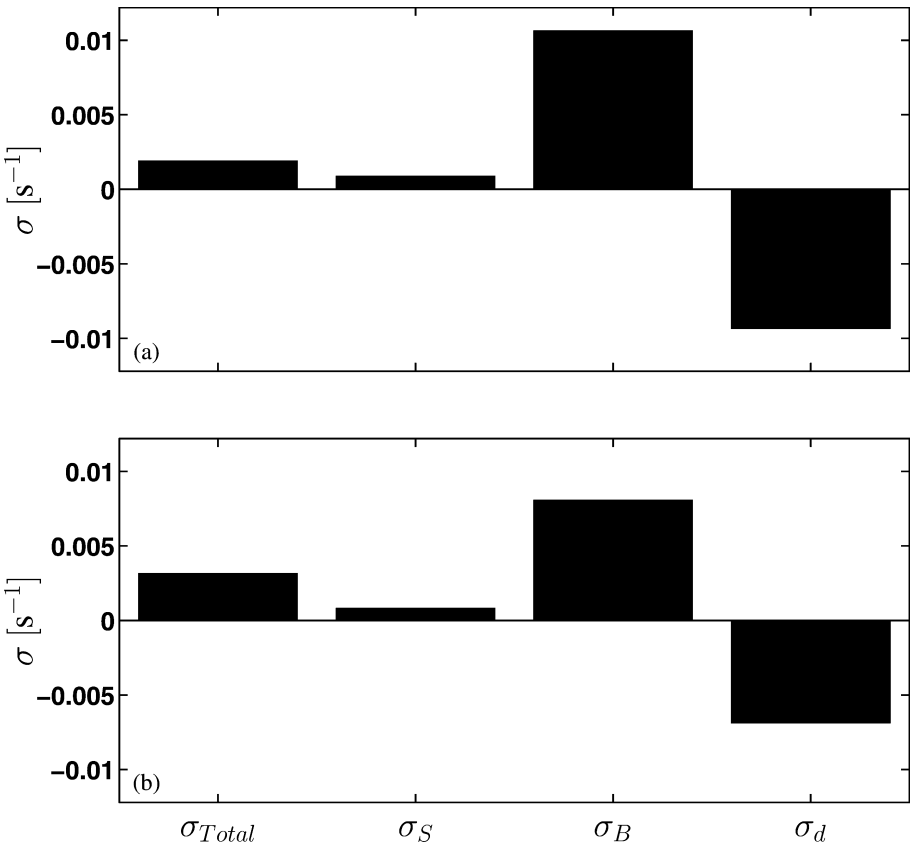

Figure 12. Partial growth rates of perturbation kinetic energy budget of the zig-zag mode (a) and tip mode (b).

results, i.e. it is not an artifact of either linearization or the frozen flow approximation. This may explain why parameterizations based on the disruption of salt fingers by shear-driven instabilities have had difficulty predicting observed fluxes (e.g. Inoue *et al.*, 2008).

Secondary instabilities and the development of salt-fingering turbulence in various regimes of stratification and shear are explored in Smyth and Kimura (2011) and Kimura *et al.* (2011) via direct numerical simulations. Shear effects in the regime of diffusive convection remain to be explored.

Acknowledgments. Comments from two anonymous reviewers improved the manuscript. This project has benefited from discussions with Eric Kunze and Bill Merryfield. The work was supported by the National Science Foundation under Grant No. 0453140.

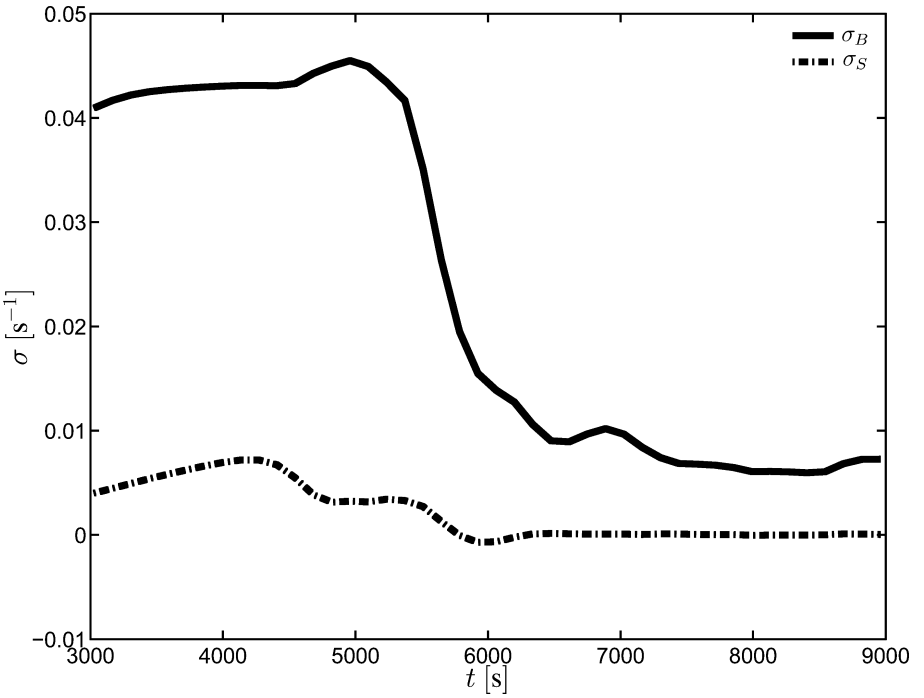

Figure 13. Evolution of partial growth rates of shear and buoyancy productions from DNS after $t = 3030$ s.

REFERENCES

Anderson, E., Z. Bai, C. Bischof, S. Blackford, J. Demmel, J. Dongarra, J. D. Croz, A. Greenbaum, S. Hammarling, A. McKenney, and D. Sorensen. 1999. LAPACK User's Guide. Third Edition, SIAM, Philadelphia.

Gargett, A. E., W. Merryfield, and G. Holloway. 2003. Direct numerical simulation of differential scalar diffusion in three-dimensional stratified turbulence. J. Phys. Oceanogr., *33*, 1758–1782.

Gregg, M. and T. Sanford. 1987. Shear and turbulence in thermohaline staircases. Deep-Sea Res., *34*, 1689–1696.

Hazel, P. 1972. Numerical studies of the stability of inviscid parallel shear flows. J. Fluid Mech., *51*, 39–62.

Holyer, J. 1984. The stability of long steady, two dimensional salt fingers. J. Fluid Mech., *147*, 169–185.

—— 1985. The stability of long steady, three-dimensional salt fingers to long-wavelength perturbations. J. Fluid Mech., *156*, 495–503.

Inoue, R., E. Kunze, L. S. Laurent, R. Schmitt, and J. Toole. 2008. Evaluating salt-fingering theories. J. Mar. Res., *66*, 413–440.

Kimura, S. and W. Smyth. 2007. Direct numerical simulation of salt sheets and turbulence in a double-diffusive shear layer. Geophys. Res. Lett., *34*, L21610.

Kimura, S., W. Smyth, and E. Kunze. 2011. Turbulence in a sheared, salt-fingering-favorable environment: Anisotropy and effective diffusivities. J. Phys. Oceanogr., *41*, 1144–1159.

Kunze, E. 2003. A review of oceanic salt fingering theory. Prog. Oceanogr., *56*, 399–417.
—— 1987. Limits on growing finite-length salt fingers: A Richardson number constraint. J. Mar. Res., *45*, 533–556.
Kunze, E., A. Williams, and R. Schmitt. 1987. Optical microstructure in the thermohaline staircase east of Barbados. Deep-Sea Res., *34*, 1697–1704.
Linden, P. 1974. Salt fingers in a steady shear flow. Geophys. Fluid Dyn., *6*, 1–27.
Proctor, M. R. E. and J. Holyer. 1986. Planform selection in salt fingers. J. Fluid Mech., *168*, 241–253.
Schmitt, R. W. 2003. Observational and laboratory insights into salt finger convection. Prog. Oceanogr., *56*, 419–433.
—— 1994. Triangular and asymmetric salt fingers. J. Phys. Oceanogr., *24*, 855–860.
Shen, C. 1995. Equilibrium salt-fingering convection. Physics of Fluids, *7*, 706–717.
Smyth, W. D. and S. Kimura. 2007. Instability and diapycnal momentum transport in a double-diffusive stratified shear layer. J. Phys. Oceanogr., *37*, 1551–1565.
—— 2011. Mixing in a moderately sheared, salt fingering layer. J. Phys. Oceanogr., *41*, 1364–1384.
Smyth, W. D., J. Nash, and J. Moum. 2005. Differential diffusion in breaking Kelvin-Helmholtz billows. J. Phys. Oceanogr., *35*, 1044–1022.
Stern, M. 1960. The 'salt fountain' and thermohaline convection. Tellus, *12*, 172–175.
—— 1969. Collective instability of salt fingers. J. Fluid Mech., *35*, 209–218.
—— 1975. Ocean Circulation Physics, Academic Press, NY, 246 pp.
Stern, M., T. Radko, and J. Simeonov. 2001. Salt fingers in an unbounded thermocline. J. Mar. Res., *59*, 355–390.
Stern, M. and J. Simeonov. 2005. The secondary instability of salt fingers. J. Fluid Mech., *533*, 361–380.
Traxler, A., S. Stellmach, P. Geraud, T. Radko, and N. Brummell. 2011. Dynamics of fingering convection. Part 1 Small-scale fluxes and large-scale instabilities. J. Fluid Mech., *677*, 530–553.
Veronis, G. 1987. The role of the buoyancy layer in determining the structure of salt fingers. J. Fluid Mech., *180*, 327–342.
Winters, K., J. MacKinnon, and B. Mills. 2004. A spectral model for process studies of rotating, density-stratifed flows. J. Atmos. Oceanic Technol., *21*, 69–94.

Received: *9 February, 2009*; revised: *29 August, 2011*.